MATERIALS SCIENCE

Direct approach to high-resolution, square-lattice alternating nanodot array by breaking hexagonal symmetry of block copolymer spheres

Seong Eun Kim¹†, Gabriella P. Irianti²†, Hyunwoo Kim³, Vikram Thapar², Hyeongoo Kim³, Jungki Ryu³*, Su-Mi Hur²*, So Youn Kim¹*

Expanding the morphological spectrum of block copolymer (BCP) self-assembly remains a notable challenge in BCP-based bottom-up nanofabrication. We present a simple method to fabricate unconventional yet crucial structures of sphere-forming BCPs in thin films using solvent vapor. By precisely controlling solvent uptake, we transform the final lattice structure of spheres, modifying the thermodynamically stable lattice of BCPs. Molecular dynamics simulations reveal that increased solvent uptake elongates the spheres, raising interfacial energy and causing sphere splitting. The additional layers generated from the sphere splitting present a nonconventional lattice, typically not observed in thin films. Using these structures, we fabricate bimetallic nanodot arrays, where two different metal components are positioned alternatingly. This array exhibits higher catalytic activities compared to the homometallic nanopatterns, with the ultralow mass of noble metals below 300 nanograms per square centimeter, highlighting their potential as electrochemical catalyst platforms.

Copyright © 2025 The Authors, some rights reserved; exclusive licensee American Association for the Advancement of Science. No claim to original U.S. Government Works. Distributed under a Creative Commons Attribution NonCommercial License 4.0 (CC BY-NC).

Check for updates

INTRODUCTION

Nanopatterning has been a keystone in nanotechnology and has helped to revolutionize various fields of science and engineering, with the ability to construct structures at the nanoscale. Despite its revolutionary impact, challenges in maintaining the pace of improvements in device performance have emerged in recent years (1). The primary issue lies in the current "top-down" process, which often struggles to maintain fine patterning accuracy, resulting in significantly increased processing costs. Consequently, there is a growing demand for nanopatterning techniques to efficiently produce nanopatterns with enhanced precision.

Nanopatterning with block copolymers (BCPs) has been considered a promising method for decades based on its simple and versatile "bottom-up" approach (2). BCPs naturally self-assemble, creating well-ordered nanostructures. BCPs have a broad morphology spectrum from simple structures (e.g., sphere, cylinder, and lamellar) (3) to more complex ones (e.g., mesh, perforated lamellar, and plumber's nightmare) (4–7), attracting scientists to explore them fundamentally and practically. BCPs have served as versatile materials as templates for fabricating metallic or inorganic nanostructures based on their ability to generate more complex nanostructures with fewer processing steps (8–10).

However, sphere-forming BCPs typically form hexagonal closepacked (hcp) lattices, limiting diversity, while nonconventional lattices like square arrays are crucial for advanced nanopatterning (11).

Considering BCPs as platforms for studying fundamental phenomena of metals or inorganics, the absence of nonconventional lattice structures prevents an exploration beyond the accessible structure (12, 13). Altering BCP lattice structures requires complex,

resource-intensive designs of polymer blocks or substrates (14, 15), reducing practicality. Furthermore, to implement BCP self-assembly at the device level, it is crucial to integrate it with existing directed self-assembly methods to achieve long-range order and reduced defectivity. In this context, there is a strong need for a simple experimental approach that enables access to nonconventional yet highly ordered structures.

In this study, we provide a strategy to form a nonconventional lattice structure of BCP in a large area with unprecedented simplicity. We first report the discovery of the solvent-assisted lattice transition of sphere-forming BCPs and then demonstrate their capability to fabricate unpreceded metallic nanopatterns with exquisite precision. Figure 1 demonstrates the suggested experimental strategy. several layers according to the swelling ratio (SR), transiting their stable lattice structure. The stable has been stable lattice. stable lattice structure. The stable hcp lattice structure in thin films transforms into a face-centered orthorhombic (fco) lattice at higher SR. Molecular dynamics (MD) simulations also reveal lattice transitions probing the local interfacial energy changes. Our discovery of different lattice structures in thin films enables the formation of various nonconventional nanopatterns on a wafer scale. We broaden the sets of nanopatterns ranging from hexagons to squares using hcp and fco lattice as a template. This simple approach produces bimetallic nanodot arrays, where two different metal components are alternatingly positioned. We further explored the use of nanopatterns in electrochemical hydrogen evolution reaction (HER) and found that the bimetallic nanodot array has higher catalytic activities compared to the homometallic nanopatterns.

RESULTS

SR-dependent in-plane structural evolution

To investigate the *SR*-dependent structural transition of BCP, we used polystyrene-*b*-poly(2-vinyl pyridine) with a molecular weight of 88-*b*-18 kg/mol (PS-*b*-P2VP, SV8818) at a thickness of 80 nm. The solvent vapor annealing was conducted in a customized chamber

¹Department of Chemical and Biological Engineering, Institute of Chemical Processes, Seoul National University, Seoul 08826, Republic of Korea. ²School of Polymer Science and Engineering, Chonnam National University, Gwangju 61186, Republic of Korea. ³School of Energy and Chemical Engineering, Ulsan National Institute of Science and Technology, Ulsan 44919, Republic of Korea.

^{*}Corresponding author. Email: jryu@unist.ac.kr (J.R.); shur@jnu.ac.kr (S.-M.H.); soyounkim@snu.ac.kr (S.Y.K.)

[†]These authors contributed equally to this work.

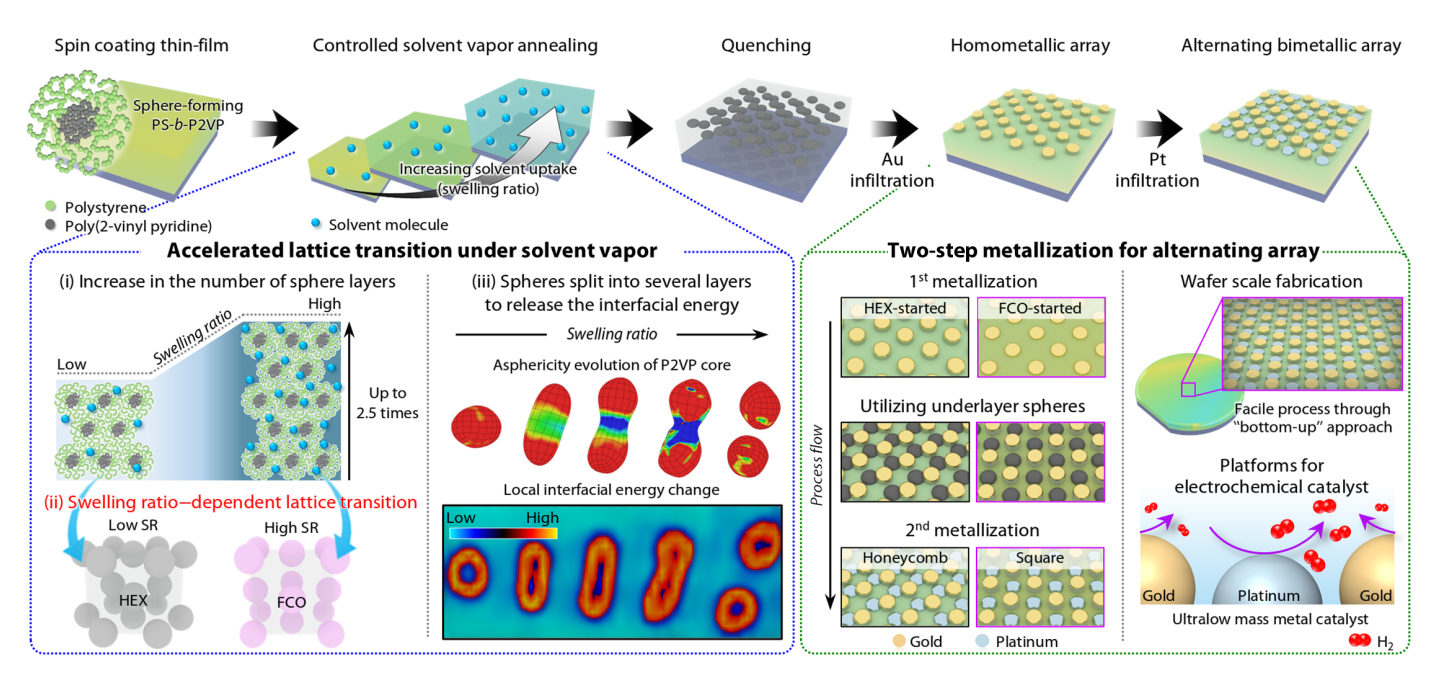


Fig. 1. Fabrication of alternating bimetallic array using solvent-assisted lattice transition of sphere-forming BCPs.

equipped with ellipsometry for in situ monitoring of the film thickness (*t*). The in situ grazing-incidence small-angle x-ray scattering (GISAXS) was also performed to examine the structural change.

Figure 2A shows the continuous increment of SR with time during the solvent vapor annealing. The swelling accompanies the micrometer- scale structural rearrangement referred to as hole-i sland behavior (16) confirmed with their optical microscope (OM) images (insets in Fig. 2A). Figure 2B presents the in situ GISAXS analysis probing the nanometer- scale structural arrangement with increasing SR (or times). At the initial annealing stage (up to 32 mins), Bragg's first- order peak appears with a peak ratio 1: 3^{0.5}: 2... indicating a hexago-nal structure. As swelling progresses, the unusual in-plane structure is observed; the peak splits into two different peaks labeled q_1 and q_2 in the "40 min" in Fig. 2B, maintained even after rapid solvent re-moval. The maintained Bragg's peaks indicate that the solvent re-moval step occurred rapidly (less than 3 s in our case), thus, allowing shrinkage predominantly along the z axis while preserving in-plane structural arrangement.

We further examined the change of in-plane nanostructures in detail through scanning electron microscopy (SEM) image analysis. Figure 2C shows the binarized SEM images at each SR with twodimensional (2D) fast Fourier transformation (2D-FFT) profiles. At relatively low SR (up to SR = 2.2), 2D-FFT peaks were found with a 1: 3^{0.5}: 2... ratio, confirming the regular hexagonal lattice again (fig. S1). However, additional peaks with slightly different orientations appeared at higher SR (above 2.3) in the 2D profiles. To identify the origin of these peaks, we calculated the degree of distortion from the regular hexagon. Figure 2D illustrates angular deviations from 60° within each unit cell, visualized as a color map. (fig. S2; further details are in the Supplementary Materials). At low SR, the images are yellowish reflecting hexagonal arrays, with partial blue at grain boundaries or defects. At higher SR (above 2.3, island), the overall color shifts to blue, suggesting the emergence of a nonhexagonal structure and a uniform structural distortion.

The deformation of the lattice structure is further examined by the angle distribution in unit cells (Fig. 2E). The angle distributions at lower *SR* are well fitted with a single Gaussian curve with a peak at 60°; however, at higher *SR* (above 2.3, island), they become broad splitting into the summation of two Gaussians. The lattice transition is most clearly found at *SR* 2.5 where two dominant peaks are located at 56° and 67°, deviated from the 60°. The area of 56° is nearly twice that of 67°, suggesting an equilateral triangle in the hexagonal unit cell deforms to an isosceles triangle at higher *SR*.

The distortion of the unit cell angle (ϕ) was calculated using 1D profiles extracted from the 2D-FFT (fig. S1) to investigate the inplane structural transition. The q_1 and the q_2 found in the reciprocal space are related to ϕ as written in Eq. 1

$$\phi = \cos^{-1}\left(\frac{q_2}{2q_1}\right) \tag{1}$$

Figure 2F presents the ϕ variation with SR showing a noticeable drop to 57° at SR 2.5, consistent with real space analysis in Fig. 2E, and the d-spacing also splits into d₁ and d₂ for q_1 and q_2 , respectively. When the SR reaches too high (above 2.8), peaks dissipate because BCPs experience the order-disorder transition (17). We also note that the overall d-spacing slightly increases and decreases back with SR due to the screening effect of solvent molecules, similar to the previous reports indicating its insensitivity to the lattice transition (18). The comprehensive in-plane structural analyses confirm that the lattice transition occurs at a sufficiently high SR, and the regular hexagon deforms to a slightly stretched hexagon with roughly 7% difference between d₁ and d₂ as illustrated in Fig. 2G.

SR-dependent out-of-plane structural evolution

After confirming the in-plane transition, we examined the out-of-plane lattice structure with the 3- d_1 thickness film. The films were vapor-annealed at several different SRs (fig. S6), and their out-of-plane (interlayer) domain spacing (d_{inter}) in the swollen state was

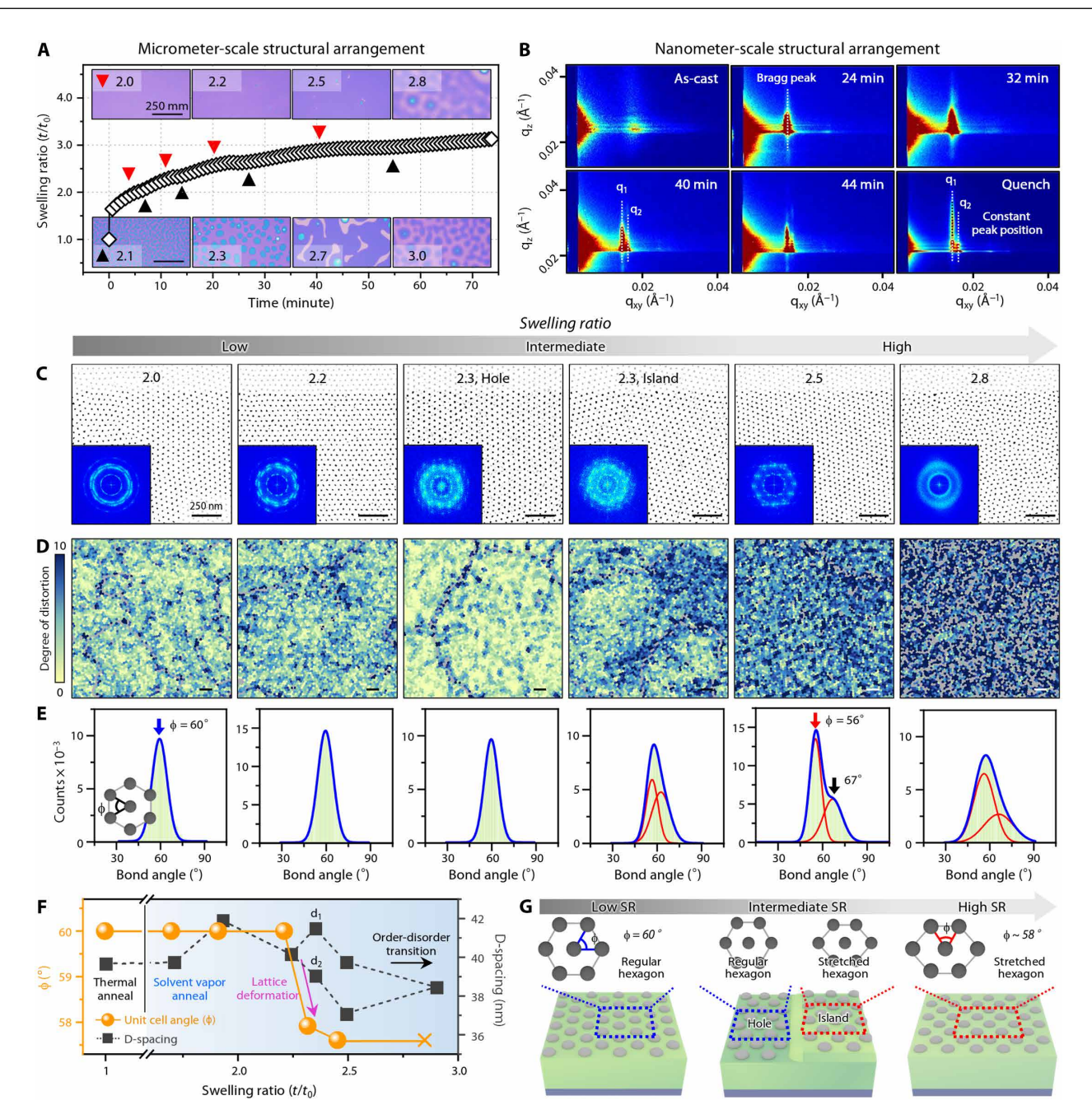


Fig. 2. In-plane structure analysis with increasing SR. (A) SR profile during the in situ monitoring by ellipsometry. Inset images are OM images trapped at local mean squared error (fig. S3) minima (red triangle, top) and maxima (black triangle, bottom). (B) In situ GISAXS 2D profiles during the solvent vapor annealing. (C) SEM images trapped at each SR. Insets are corresponding 2D-FFT profiles. (D) Color maps of the calculated degree of distortion from regular hexagon for each unit cell and (E) distribution of all angles in unit cells. (F) Calculated ϕ (orange) and d-spacing (black) by 2D-FFT. (G) Schematic illustration of transition of lattice structure with increasing the SR.

calculated with the time-of-flight secondary ion mass spectroscopy (TOF-SIMS) depth profiling by dividing the swollen thickness by the number of layers. (fig. S6 and details are in the Supplementary Materials). Figure 3A presents the variation of the d-spacing for in and out of plane; the variation in d_{inter} closely matches the trend and lengths of the in-plane domain spacing (d_1 and d_2).

When the BCPs are swollen, they incur energetic penalties, making it challenging to maintain the original layers. To alleviate this, they rearrange their chains to form additional layers, as shown in Fig. 1(i). However, forming new lattice layers reduces chain density

in the spheres. At excessively high *SR*, the chain density becomes too low to sustain the lattice structure. We found that BCPs can maintain the lattice up to around *SR* 2.5 (fig. S6C).

Identification of the lattice structure and its transition pathway

The lattice transition pathway was investigated using ex situ GISAXS experiments. Films with thicknesses ranging from 1 to 19- d_1 were prepared via spin-coating, followed by solvent vapor annealing at $SR \sim 2.4$ and rapid solvent removal to trap the structure.

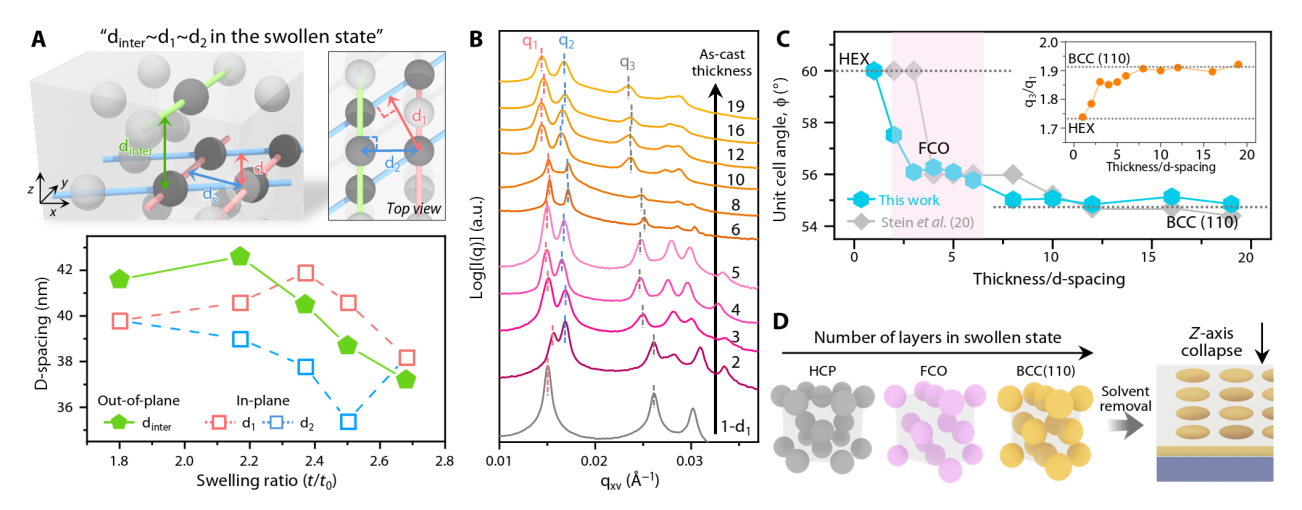


Fig. 3. Out-of-plane structure analysis according to the SR and exploration of transition pathway through ex situ GISAXS. (A) Calculated interlayer domain spacing (d_{inter} , green) using TOF-SIMS depth profiling and in-plane domain spacing (red for d_1 and blue for d_2). (B) Ex situ GISAXS 1D profiles after solvent annealing. Film thickness is from 1- to 19- d_1 thickness, and SR is around 2.4. (C) Calculated ϕ by q_1 and q_2 peak positions for each sample (blue hexagon) and ϕ from Stein *et al.* (20) (gray). Dashed lines are ideal values of hcp (top) and bcc (100) lattices (bottom). Inset is the ratio between q_4 and q_7 for each sample. (D) Schematic illustration of lattice structure with increasing the number of layers in swollen state and after solvent removal. a.u., arbitrary units.

The 1D scattering profile in Fig. 3B shows shifts in q_1 and q_2 positions with increasing thickness. Using Eq. 1, the ϕ was calculated to evaluate the in-plane lattice structure, as presented in Fig. 3C (blue). The ϕ is 60° at 1-d₁, corresponding to the hcp lattice, but it immediately drops at 2-d₁ thickness. It reaches 56° at 3 to 5-d₁ thickness then further decreases to 54.7° at 8-d₁ thickness, aligning with the (110) plane of a body-centered cubic (bcc) lattice. The calculated q_3/q_1 ratio from Fig. 3B follows the same trajectory (Fig. 3C, inset).

This distinct lattice transition with increasing thickness has been previously reported with the thermal annealing of lower molecular weight PS-b-P2VP (19, 20). Figure 3C compares the solvent vapor annealing results from this study with thermal annealing data (gray) from the literature. In thermal annealing, the hcp lattice deforms discontinuously into fco packing at four to five layers, transitioning from a 2D to a 3D lattice. In both cases, the fco structure acts as an intermediate phase between hcp and the bcc(110) plane, with an angle of $\varphi \sim 56^\circ$. Figure 3C also shows that solvent vapor annealing induces fco formation and promotes non-hcp lattices in thinner films, accelerating the lattice transition. This acceleration occurs independent of the molecular weight of BCP and solvent. Figures S5 and S6 show the emergence of fco transition with lower molecular weight of PS-b-P2VP and different solvent mixtures.

The lattice transition to fco was further confirmed by examining the underlying layers. The projection of the lower fco layer onto the top layer revealed a stacked structure with a rectangular-like pattern, indicating two fco layers (fig. S9). GISAXS measurements (fig. S10) and bottom-view SEM imaging (fig. S11) further confirmed that the fco lattice extends throughout the film, demonstrating stable transitions from hcp to fco in the swollen state. These structures are readily trapped by the rapid solvent removal, inducing a structural collapse along the *z*-axis direction (Fig. 3D).

Splitting mechanism through the molecular dynamics (MD) simulations

To explore the morphological evolution of sphere-forming BCP films, we conduct coarse-grained MD simulations of solvent vapor annealing on a free-standing thin film. We simulate solvent uptake

by decreasing the chain density from melt condition to half of its initial value, achieving an SR (= ρ/ρ_0) of 2, while treating solvent implicitly. PS (P2VP) was treated as a B(A) block. The system mimics PS-b-P2VP behavior, where the majority B block preferentially wets the free surface, and the solvent swells both A and B blocks equally. Details are provided in Materials and Methods. In Fig. 4C, simulation snapshots, taken from the diagonal slice of the simulation box, capture both the swelling process and the following morphology transitions. Initial single-layer spheres undergo deformation and elongation, eventually splitting into two layers as the SR increases. This transition is quantified by analyzing the number of spheres and their average asphericity. Density-based spatial clustering of applications (DBSCAN) with noise algorithm is used to delineate the contour points of type-A density fields, as detailed in fig. S13.

Figure 4A plots the number of spherical clusters (green) and the fraction of these clusters exhibiting high asphericity above a threshold value of 0.05 (orange) against the *SR*. Initially, most spheres exhibit low asphericity, resembling perfect spheres. As *SR* approaches 1.2, the fraction of highly aspherical spheres increases significantly, peaking above 0.5, while the total number of spheres remains unchanged, indicating primary elongation of spheres during this phase. With further increases in *SR*, the fraction of highly aspherical spheres decreases, coinciding with an increase in the number of spheres. This suggests that the elongated spheres begin to split, forming new spheres and reducing overall asphericity. These morphological transitions are portrayed through snapshots of an isolated sphere in Fig. 4A. For enhanced clarity, these snapshots are color-coded on the basis of Gaussian curvature analysis.

As shown in Fig. 4A, the number of spheres only increases from 50 at SR 1.0 to 75 at SR 2.0, indicating partial splitting. To examine how this affects the lattice structure of spheres, we estimate intersphere distance (L_0), angles (Φ), and five/sevenfold defect counts at both early and later stages of annealing using Voronoi tessellations, detailed in fig. S11C. The progression of Φ (red diamond in Fig. 4B) maintains a consistent average value of approximately 60°, characteristic of hexagonal structure, with minor deviations shown by the error bars. This consistency supports the notion that while additional

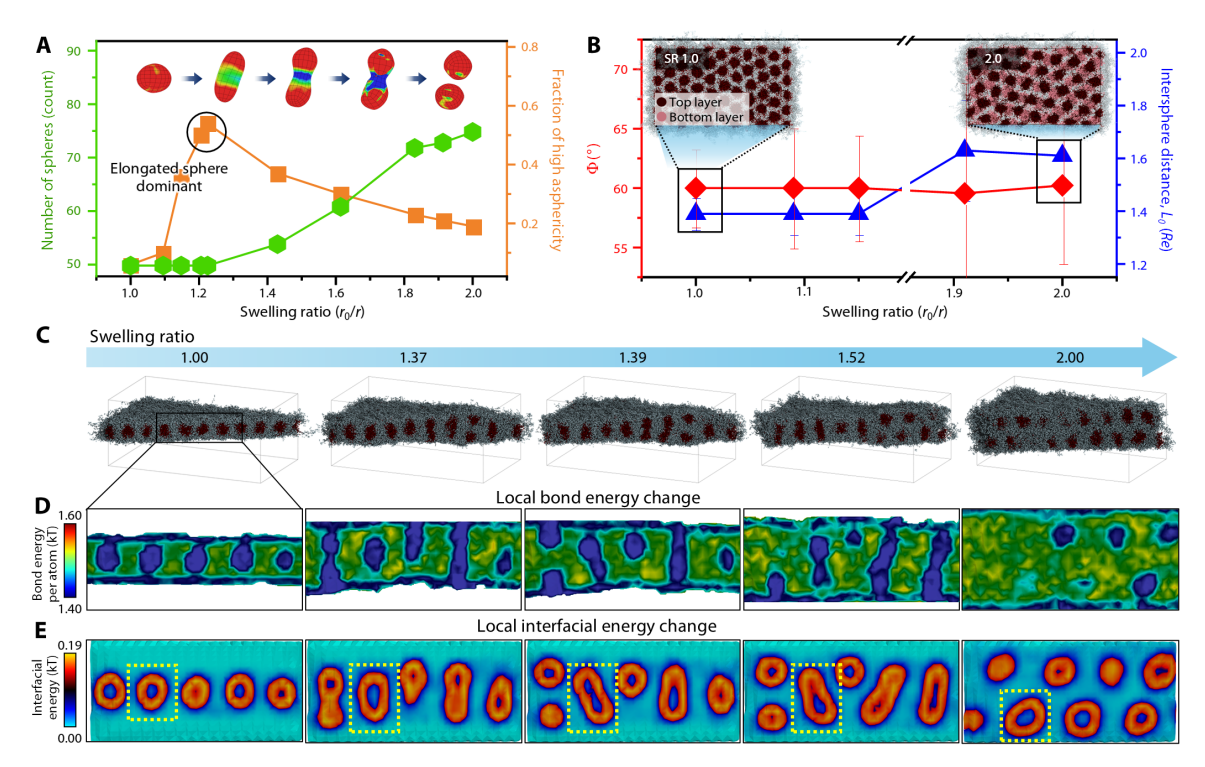


Fig. 4. MD simulation and analysis on the sphere swelling system. (**A**) Clustering analysis on number of spheres and fraction of spheres with high asphericity value through different *SR*. (**B**) Line plot of average angles and periodicity length (*L*₀) of sphere domains through different *SR*. (**C**) Simulation snapshots of the swelling process taken from a cut of diagonal perspective. (**D**) Local bond energies corresponding to simulations snapshots. (**E**) Local interfacial energies plot corresponding to the simulation snapshots.

layers of spheres form, each layer retains hexagonal packing, also consistent with the experimental result in Fig. 2F. The intersphere distance slightly increases as the film swells up to SR of 2.0, likely due to the decrease in the number of spheres per layer. Using Voronoi tessellation results, we identify neighboring spheres by shared vertices and count instances of non-ideal symmetry after two layers of spheres have formed (fig. S14). Figure S10 presents the number of five and sevenfold defect pairs plotted against simulation time steps during the equilibration at SR 2.0, showing a decreasing trend. In the final snapshot, all Voronoi cells exhibit sixfold symmetry, without any defect pairs present, confirming the reestablishment of a perfect hexagonal lattice. Notably, 10 times faster rapid swelling prevents spheres from adjusting their spacing, resulting in almost all spheres elongating and splitting (fig. S15A). Thus, the number of spheres during fast swelling increases sharply to 90 at SR 1.93 (fig. S15B). However, the sphere count eventually converges back to that of the slower ramping simulation, indicating some spheres coalesce to their equilibrium state at high SR, which is equal to the final state of slower swelling (fig. S16). The splitting process is provided in movie S1 increasing the SR up to 2.0 and higher.

The total energy across the entire simulation box remains stable during swelling, consistent with previous studies suggesting that subtle energy variations can significantly influence the self-assembly and morphological transitions (21). However, examination of the local energy distribution by calculating bond stretching/compression and A-B incompatibility on a grid with spacing of 0.16Re (matching the interaction length ΔL_{GL} in our model) provides insights into the sphere-splitting mechanism (Fig. 4, D and E). The results reveal that

A blocks within the spherical domains exhibit lower bond energies (blue) compared to the surrounding B blocks (green). Notably, the bond energies within the spheres remain unchanged even during sphere elongation, indicating that chain stretching is not the primary driver of sphere splitting. In contrast, the interfacial region between A and B, highlighted in orange in the incompatibility energy map, expands as spheres elongate along z direction upon swelling. While the effective segregation strength between A and B blocks decreases because of the solvent's screening effect as SR increases (22–24), the intensity of local incompatibility energy along the circumference of spheres remains constant, indicating increased mixing of A/B. This enhanced intermixing and enlarged interfacial area of elongated spheres increase interfacial energy locally and lead to energetically favorable spheres splitting.

However, as highlighted by the yellow box in Fig. 4E, we observe cases where spheres recover their spherical shape without splitting, particularly prevalent when neighboring spheres have already undergone splitting. This behavior matches with the sphere counts in Fig. 4A and additional analysis on the sphere volume variation during swelling in fig. S17A. Sphere volume variations initially increase with SR, whereas they notably decrease at SR 2.0, confirming uniform sphere sizes at high SR. This occurs because, at high SR, the solvent-induced reduction in segregation strength (χ) between A and B blocks facilitates chains redistribution between phases, leading to size equalization among spheres (fig. S17B). This hypothesis is further confirmed by simulations with higher initial segregation strength between A and B, χN of 70 (fig. S18), which showed insufficient screening by the solvent at SR 2.0, causing the spherical

domains to maintain their elongated structures rather than undergoing splitting.

Upon quenching the system back to its initial chain density, the double-layered structure formed at high *SR* is preserved, consistent with experimental observations. As shown in fig. S16, the lateral spacing between spheres remains intact even as the *z* spacing decreases, with both layers maintaining the hexagonal packing and uniform sphere sizes regardless of whether individual spheres underwent splitting during swelling.

Fabrication of BCP-templated alternating bimetallic nanodot array

The systematic lattice variation of the BCP thin film can serve as a useful platform for generations of versatile nanopatterns and their applications. Our solvent-assisted lattice transition enables the creation of a unique alternating nanopattern, unprecedented in thin films. We used the single or stacking structure of the hcp or fco to produce multi-arrays from hexagonal to honeycomb, orthorhombic to square structures, and the processing steps of homo- and bimetal-lic arrays are demonstrated in Fig. 5A.

The first gold nanopattern in the top layer was prepared by immersing the films in HAuCl₄ aqueous solution and etching with O₂

plasma as shown in Fig. 5A (step i) (25). Then, the $\rm O_2$ plasma treatment was conducted to etch the film ~10 nm to reach the underlayer and induce a reduction reaction from $\rm Au^{3+}$ to Au (step ii) in the top layer. Next, the films were immersed in Na₂PtCl₄ aqueous solution and exposed to O₂ plasma again (step iii). The gold nanodot arrays remain stable during the second metal infiltration step, enabling the production of alternation bimetallic nanodot arrays.

Figure 5B presents the successfully patterned homo- and bimetallic arrays from the hcp and fco lattice structures. These homo- and bimetallic arrays were obtained in a large area, and the corresponding GISAXS profiles show the reinforced q_2 and $2q_1$ peaks by the doubled population of scattered particles (Fig. 5C). The bimetallic nanodot arrays were successfully generated using different metal combinations as well (fig. S19).

We further produced single-grain metallic arrays in a large area, adopting the self-directed assembly technique (26) at 2- d_1 thickness films and presented in Fig. 5D. In this process, the spheres were transformed to the guiding cylinders with shear (top image in Fig. 5D) and following solvent vapor annealing transformed cylinders into aligned spheres (bottom image in Fig. 5D). The transition of hcp to fco then occurred, producing fco lattice in a large area with a correlation length of 11 μ m (fig. S20). To demonstrate compatibility

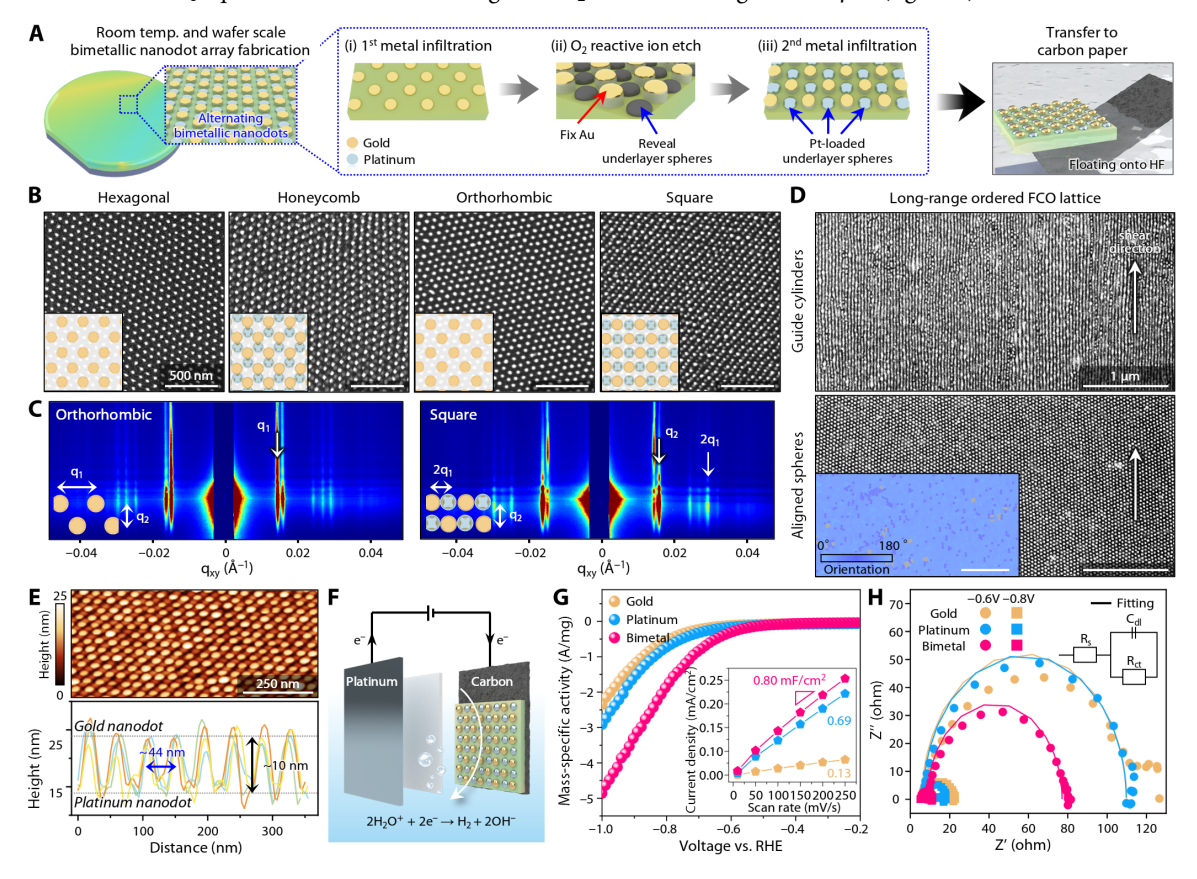


Fig. 5. Fabrication of alternating bimetallic nanodot arrays and their applications. (A) Schematic illustration of the experimental process to fabricate alternating bimetallic nanodot arrays. (B) SEM images of metal nanodot arrays for four different structures after metal infiltration and O₂ plasma treatment. (C) GISAXS 2D profiles for orthorhombic homo- and square bimetallic nanodot arrays. (D) SEM image of guide cylinders after applying shear force on SV8818 film with 2-d₁ thickness (top) and that of fco structure in a large area after solvent vapor annealing (bottom). Inset is the orientation map of spheres. The direction of the shear force is marked as white arrows. (E) Atomic force microscope image and corresponding height profile of square array. Height profiles were extracted from four different parts, and the average heights of each metal component are marked as dashed lines. (F) Schematic illustration of HER. (G) Polarization curves for electrochemical HER on gold (yellow), platinum (blue), and bimetallic (pink) nanodot arrays in 1 M KOH electrolyte. Inset shows the results of electrochemically active surface area measurements. (H) Electrochemical impedance spectroscopy for each sample with fitted curves (solid lines). Inset shows corresponding equivalent circuit.

with current-directed self-assembly method, we generated unidirectionally aligned alternating array combining with graphoepitaxy. Figure S21 shows that the alternating array is successfully fabricated inside trenches aligned along the trench direction. In this regard, our approach enables simple yet highly controlled fabrication of bimetallic nanodot arrays. Notably, we achieve a square pattern without any external templating or treatment, thereby bypassing the conventional requirement for complex processing to overcome the thermodynamic instability typically associated with square arrays (27-29). Furthermore, the stacked structure of sphere-forming BCPs enables selective infiltration to each layer, accessing alternating nanodot arrays improving the resolution limit and regioselectivity (30, 31). Rapid solvent removal compressed the lattice in the z direction, and subsequent metal incorporation produced highly collapsed bimetallic structures with a height difference of ~10 nm (Fig. 5E), enabling the exploration of synergetic effects in confined spaces.

Different metal species demonstrated a synergistic effect on catalytic activity. To evaluate the HER efficiency under alkaline conditions, orthorhombic homo- and square bimetallic nanopatterns were transferred onto carbon paper (Fig. 5, A and F). Among these, the alternating bimetallic nanodot array exhibited the highest mass-specific activity for HER, surpassing homometallic counterparts (Fig. 5G). The superior performance was consistently confirmed through various bimetallic combinations, including Au-Pt and Pd-Pt structures (Fig. 5G and fig. S22), highlighting the general synergistic effects in bimetallic nano patterns. To examine the influence of lattice geometry, we compared HER performance between Au-Pt nanodot arrays with square and honeycomb arrangements. The square arrangement exhibited higher catalytic activity, suggesting that lattice geometry affects HER performance (fig. S23).

We further verified that the catalytic enhancement is not due to metal mixing or unintended alloying. In the scanning transmission electron microscopy-energy dispersive x-ray spectroscopy (STEM-EDS) mapping, the exact position of each element is ambiguous since the low mass of loaded metals and peak position between Au and Pt is indistinguishable (fig. S24). For this reason, we prepared the control sample alloying Au and Pt in both first and second layer (fig. S25). Figure S23C shows that alloyed AuPt-AuPt shows lower HER activity than the bimetallic nanodot array, indicating that controlled bimetallic structure is essential for optimal performance. Electrochemically active surface areas of platinum and the bimetallic nanodot array were comparable (inset of Fig. 5G), excluding the possibility that enhanced performance was due to a higher surface area. Furthermore, the bimetallic nanodot array showed higher mass-specific activity than Pt/C, a benchmark HER catalyst (fig. S26 and table S2). The long-term stability of the catalyst was also confirmed by cyclic voltammetry, which showed not only sustained performance but also a gradual increase in activity likely due to electrochemical activation via crystallization (32) or surface reconstruction (fig. S27) (33).

Electrochemical impedance spectroscopy further confirmed the exceptional performance of the bimetallic nanodot array (Fig. 5H). While the solution resistance (R_s) was consistent across all catalysts, the charge transfer resistance (R_{ct}) was significantly reduced in the bimetallic nanodot array (table S3). These findings align with previous reports on the high catalytic activity of bimetallic catalysts (34, 35) and provide insights into the design and synthesis of electrocatalysts with minimal use of noble metals, which is unavoidable for practical application due to their outstanding activity and stability (36). Our

current catalyst is supported by PS, which is an electrical insulator causing higher applied voltage. Therefore, catalytic activity has the potential to be improved by modifying PS matrix, e.g., mixing with conductive molecules or physical removal. We expect high catalytic activity to be achieved comparable to commercial electrochemical catalyst by increasing electron conductivity of support.

DISCUSSION

In this study, we achieved a nonconventional, non-hcp lattice structure that deviates from the thermodynamic stable structures found in thin films. We explored how the stable lattice structure transforms under solvent vapor atmospheres, revealing that the emergence of the fco structure results from accelerating lattice transitions, facilitated by an increased number of spherical layers. On the basis of the transition mechanisms revealed with MD simulations, we additionally proposed the experimental strategy for bottom-up nanofabrication process, enabling the production of multiple nanopatterns, including hexagonal to square configurations. We successfully produced alternating bimetallic nanodot arrays of these structures on a wafer scale, demonstrating their possibility as electrocatalyst. To the best of our knowledge, this represents previously unprecedented fabrication of alternating bimetal nanodot arrays. We believe our study offers valuable insights into the fundamental nature of self-assembly in BCPs and opens opportunities for exploration in nanofabrication.

MATERIALS AND METHODS

BCP thin film preparation

PS-b-P2VP with molecular weight 88,000-b-18,000 kg/mol (\mathcal{D} =1.07) was purchased from Polymer Source Inc. PS-b-P2VP was spin-coated on the bare Si substrate with toluene solution (1.4 to 8.0 wt %). The film thickness was measured using a spectroscopic ellipsometer (M-2000V, J.A. Woollam Co.) after spin coating. For the MSE curve during the solvent vapor annealing, the same ellipsometer was used with a customized vapor annealing chamber. Otherwise, the solvent vapor annealing was conducted using reflectometry (F20-UV, Filmetrics). Toluene (anhydrous, 99.8%), tetrahydrofuran (99.0%), acetone (99.8%), and hydrochloric acid (35.0%) were purchased from Daejung Chemicals & Metals.

Alternating bimetallic nanodot array fabrication

To create the nanodot array in a large area, shear stress was applied for 30 min at 170°C to the as-cast films. The shear force was 30 kPa through the elastomer. The elastomer was a polydimethylsiloxane pad prepared with a SYLGARD 184 kit (Dow). The films were metalized by immersion in 5 mM gold precursor (platinum or palladium) aqueous solution with 1.5 wt % hydrochloric acid followed by reactive ion etching with O_2 plasma for 8 s using scientific engineering RIE-150. Gold(III)chloridetrihydrate(99.995%),sodiumtetrachloroplatinate(II) hydrate (\leq 49.8% Pt), and potassium tetrachloropalladate(II) (99.99%) were purchased from Sigma-Aldrich.

Scanning electron microscopy

A Carl Zeiss Supra 55VP and Carl Zeiss Auriga field-emission SEM (high vacuum, 2 keV) were used. For the SEM imaging, the samples were immersed in ethanol or gold aqueous solution for 1 hour otherwise noted. SEM image–based image analysis was conducted using MATLAB from The MathWorks Inc.

Atomic force microscopy

Atomic force microscope images were obtained by Park Systems NX-10 with a scan area of 2 μm by 2 μm .

Time-of-flight secondary-ion mass spectroscopy

For depth profiling, the TOF-SIMS IONTOF TOF-SIMS 5 instrument was used. The ToF-SIMS measurements were carried out with Bi₃⁺ (30 keV, 0.7 pA) with an area of 100 μ m by 100 μ m and an Arcluster beam (2.5 keV, 0.9 nA) was used to sputter the sample with an area of 400 μ m by 400 μ m.

Ex situ and in situ GISAXS

The in situ and ex situ GISAXS measurements were performed at the 3C SAXS I beamline of the Pohang Accelerator Laboratory in Korea. The energy of the x-ray was 11 keV, and the sample-to-detector distance was 3952.63 mm. The incident angle varied from 0.10° to 0.14°.

For the in situ GISAXS measurement during the solvent vapor annealing, samples were annealed using tetrahydrofuran using customized vapor annealing chamber at the beamline. To avoid damage by the x-ray, data were collected from five different areas in the same sample. Because of the lack of experimental setup, the film thickness was not provided.

Molecular dynamics

Initialization and equilibration

We conducted MD simulations of solvent vapor annealing of a monolayer thin film consisted of asymmetric AB diblock copolymers with 48 coarse-grained beads per chain. Detailed description of the coarsegrained simulation model is provided in section SI. To achieve spherical domain formation, the fraction of minority A beads $f_A = 0.14$ and the Flory-Huggins parameter $\chi N = 50$. The initialization was done by randomly placing polymer chains in a thin film of $L_z = L_0 = 1.4$ Re at the center of a box with thickness 10 Re to create sufficient empty space of implicit solvent. The box dimensions in the lateral axes are $L_x = 12.1244 \text{ Re}, L_y = 7 \text{ Re}$. This box size corresponds to the hexagonal lattice ratio of $L_x:L_y = 1: \sqrt{3}$ with $L_x = n \times L_0$. n, the number of repeating sphere patterns along the axis, was chosen to be 5. The natural periodicity between the spherical domains according to the system's χN and chain length, $L_o = 1.4$ Re was optimized through exhaustive simulations trials. Periodic boundary conditions were applied in all three directions. Figure S8 provides the snapshot of the initial monolayer film.

Simulation system was equilibrated using Monte Carlo simulation over 1,000,000 steps. An external periodic field in the shape of a Gaussian decay function was applied to guide the spherical domain into a precise hexagonal packing (*37*). The system was further equilibrated without the applied field for an additional 1,000,000 simulation steps.

Solvent annealing simulation

The virial coefficients for conditions where the vapor phase osmotic pressure is vanishingly small, $P \approx 0$, can be expressed in terms of chain density and inverse compressibility as follows (38)

$$\nu_{pp} = -2 \frac{(\kappa N + 3)}{\sqrt{\overline{N}}} \tag{2}$$

$$\omega_{ppp} = \frac{3}{2} \frac{(\kappa N + 2)}{\sqrt{N^2}} \tag{3}$$

$$\nu_{AB} = \frac{\chi N}{\sqrt{\overline{N}}} + \frac{\nu_{AA} + \nu_{BB}}{2} \tag{4}$$

where p represent the A or B type, for the crossed term $\omega_{AAB} = (2 \times \omega_{AAA} + \omega_{BBB}) / 3$ and $\omega_{BBA} = (2 \times \omega_{BBB} + \omega_{AAA}) / 3$. The inverse compressibility (κN) was chosen to vary between components, 350 for sphere phase A blocks and 50 for the matrix phase B blocks. This variation in κN , which correlates with surface tension, ensures $\gamma_B < \gamma_A$, thus selective wetting of B block at the free surface, while the A blocks, which form the spheres, remain suspended in the middle of the film. Chain density \sqrt{N} is controlling the number of chains that a given chain interacts with over a volume region and is defined as $\sqrt{N} = \rho_0 Re^3 / N$. As explored in previous studies, the melt condition corresponds to 128 chains/ Re^3 (39, 40).

Modeling a solvent annealing process with nonpreferential solvent was done by progressively ramping the system toward lower chain density $\sqrt{\overline{N}}$. Starting from the prepared initial configuration, the ramping was performed in an MD simulation under canonical ensemble to monitor the dynamic evolution of morphologies during solvent vapor annealing. We continuously adjust the average chain density, $\rho(\varphi)$, from 128 to 64 chains/ Re^3 (SR from 1 to 2) over 1,000,000 simulation steps with a time step of dt = 0.001. After the continuous swelling, the system was allowed to equilibrate for a further 1,000,000 steps. Last, the system was rapidly quenched to the original chain density over a short simulation period of 10,000 steps.

Scanning transmission electron microscopy

STEM-EDS analysis was conducted using Jeol Ltd. JEM-ARM200F Cs-corrected STEM (200 kV) installed at the National Center for Inter-university Research Facilities at Seoul National University. For the STEM measurement, PS-b-P2VP was spin-coated on the Si substrate deposited by SiO $_2$ with 160-nm thickness. After solvent vapor annealing and metallization, the film was floated onto the HF aqueous solution to transfer to the copper grid (400 mesh, 62 μ m pitch).

Hydrogen evolution reaction

PS-b-P2VP was spin-coated on the Si substrate deposited by SiO $_2$ with 160-nm thickness. After solvent vapor annealing and metallization, the film was floated onto the HF aqueous solution to transfer to the carbon paper. Hydrofluoric acid (48%) was purchased from Sigma-Aldrich.

Electrochemical HER measurements were conducted using a SP-150 potentiostat (Bio-Logic Science Instruments, France) in a three-electrode system with a 1 M KOH electrolyte. Measurements were taken in a custom H-cell containing a working electrode modified with metallized nanodot films, a platinum wire counter electrode, and a Ag/AgCl reference electrode. Metallized nanodot films were prepared on carbon paper. Linear sweep voltammetry was performed at a scan rate of 10 mV/s, with a potential range of 0 to $-1.0\,\mathrm{V}$ versus the reversible hydrogen electrode (RHE). Long-term cyclic voltammetry cycle was conducted at a scan rate of 50 mV/s, with a potential range of 0 to $-0.72\,\mathrm{V}$ versus the RHE. All potentials were referenced to the Ag/AgCl and converted to the RHE scale using the Nernst equation ($E_{\mathrm{RHE}}=E_{\mathrm{Ag/AgCl}}+0.05916\times\mathrm{pH}+0.197\,\mathrm{V}$). Electrochemical impedance spectroscopy measurements were measured in the frequency range of 0.1 to $10^5\,\mathrm{Hz}$. All tests were conducted in triplicate.

Supplementary Materials

The PDF file includes:

Supplementary Text Figs. S1 to S27 Tables S1 to S3 Equations S1 to S5 Legend for movie S1 References

Other Supplementary Material for this manuscript includes the following: Movie S1

REFERENCES AND NOTES

- J. T. Fourkas, J. Gao, Z. Han, H. Liu, B. Marmiroli, M. J. Naughton, J. S. Petersen, Y. Sun, A. Vagilio Pret, Y. Zheng, Grand challenges in nanofabrication: There remains plenty of room at the bottom. Front. Nanotechnol. 3, 700849 (2021).
- R. A. Segalman, Patterning with block copolymer thin films. Mater. Sci. Eng. R. Rep. 48, 191–226 (2005).
- E. L. Thomas, R. L. Lescanec, F. C. Frank, J. S. Higgins, A. Klug, I. W. Hamley, A. Keller, M. Warner, A. H. Windle, Phase morphology in block copolymer systems. *Philos. Trans. R. Soc. London Ser. A* 348, 149–166 (1994).
- E. L. Thomas, D. B. Alward, D. J. Kinning, D. C. Martin, D. L. Handlin Jr., L. J. Fetters, Ordered bicontinuous double-diamond structure of star block copolymers: A new equilibrium microdomain morphology. *Macromolecules* 19, 2197–2202 (1986).
- Z. Sun, R. Liu, T. Su, H. Huang, K. Kawamoto, R. Liang, B. Liu, M. Zhong, A. Alexander-Katz, C. A. Ross, J. A. Johnson, Emergence of layered nanoscale mesh networks through intrinsic molecular confinement self-assembly. *Nat. Nanotechnol.* 18, 273–280 (2023).
- X. Feng, C. J. Burke, M. Zhuo, H. Guo, K. Yang, A. Reddy, I. Prasad, R.-M. Ho, A. Avgeropoulos, G. M. Grason, E. L. Thomas, Seeing mesoatomic distortions in soft-matter crystals of a double-gyroid block copolymer. *Nature* 575, 175–179 (2019).
- H. Lee, S. Kwon, J. Min, S.-M. Jin, J. H. Hwang, E. Lee, W. B. Lee, M. J. Park, Thermodynamically stable plumber's nightmare structures in block copolymers. Science 383, 70–76 (2024).
- C.-C. Liu, E. Franke, Y. Mignot, R. Xie, C. W. Yeung, J. Zhang, C. Chi, C. Zhang, R. Farrell, K. Lai, H. Tsai, N. Felix, D. Corliss, Directed self-assembly of block copolymers for 7 nanometre FinFET technology and beyond. *Nat. Electron.* 1, 562–569 (2018).
- Q. Peng, Y. C. Tseng, S. B. Darling, J. W. Elam, Nanoscopic patterned materials with tunable dimensions via atomic layer deposition on block copolymers. *Adv. Mater.* 22, 5129–5133 (2010)
- Y. S. Jung, C. A. Ross, Orientation-controlled self-assembled nanolithography using a polystyrene—polydimethylsiloxane block copolymer. Nano Lett. 7, 2046–2050 (2007).
- E. L. Thomas, D. J. Kinning, D. B. Alward, C. S. Henkee, Ordered packing arrangements of spherical micelles of diblock copolymers in two and three dimensions. *Macromolecules* 20, 2934–2939 (1987).
- 12. C. Huang, Y. Zhu, X. Man, Block copolymer thin films. Phys. Rep. 932, 1–36 (2021).
- G. S. Doerk, K. G. Yager, Beyond native block copolymer morphologies. Mol. Syst. Des. Eng. 2, 518–538 (2017).
- C. Tang, J. Bang, G. E. Stein, G. H. Fredrickson, C. J. Hawker, E. J. Kramer, M. Sprung, J. Wang, Square packing and structural arrangement of ABC triblock copolymer spheres in thin films. *Macromolecules* 41, 4328–4339 (2008).
- S. Ji, U. Nagpal, W. Liao, C. C. Liu, J. J. De Pablo, P. F. Nealey, Three-dimensional directed assembly of block copolymers together with two-dimensional square and rectangular nanolithography. *Adv. Mater.* 23, 3692–3697 (2011).
- J. N. L. Albert, T. H. Epps, Self-assembly of block copolymer thin films. Mater. Today 13, 24–33 (2010).
- R. A. Segalman, A. Hexemer, R. C. Hayward, E. J. Kramer, Ordering and melting of block copolymer spherical domains in 2 and 3 dimensions. *Macromolecules* 36, 3272–3288 (2003).
- X. Gu, I. Gunkel, A. Hexemer, W. Gu, T. P. Russell, An in situ grazing incidence x-ray scattering study of block copolymer thin films during solvent vapor annealing. Adv. Mater. 26, 273–281 (2014).
- G. E. Stein, E. W. Cochran, K. Katsov, G. H. Fredrickson, E. J. Kramer, X. Li, J. Wang, Symmetry breaking of in-plane order in confined copolymer mesophases. *Phys. Rev. Lett.* 98, 158302 (2007).
- G. E. Stein, E. J. Kramer, X. Li, J. Wang, Layering transitions in thin films of sphericaldomain block copolymers. *Macromolecules* 40, 2453–2460 (2007).
- 21. M. Müller, J. J. de Pablo, Computational approaches for the dynamics of structure formation in self-assembling polymeric materials. *Annu. Rev. Mat. Res.* **43**, 1–34 (2013).
- A. F. Hannon, W. Bai, A. Alexander-Katz, C. A. Ross, Simulation methods for solvent vapor annealing of block copolymer thin films. Soft Matter 11, 3794–3805 (2015).

- O. Dreyer, G. Ibbeken, L. Schneider, N. Blagojevic, M. Radjabian, V. Abetz, M. Müller, Simulation of solvent evaporation from a diblock copolymer film: Orientation of the cylindrical mesophase. *Macromolecules* 55, 7564–7582 (2022).
- A. A. Rudov, E. S. Patyukova, I. V. Neratova, P. G. Khalatur, D. Posselt, C. M. Papadakis,
 I. I. Potemkin, Structural changes in lamellar diblock copolymer thin films upon swelling in nonselective solvents. *Macromolecules* 46, 5786–5795 (2013).
- J. Chai, J. M. Buriak, Using cylindrical domains of block copolymers to self-assemble and align metallic nanowires. ACS Nano 2, 489–501 (2008).
- Y. C. Kim, S. Y. Kim, A single crystal 2D hexagonal array in a centimeter scale with a self-directed assembly of diblock copolymer spheres. ACS Nano 16, 3870–3880 (2022).
- C. Tang, E. M. Lennon, G. H. Fredrickson, E. J. Kramer, C. J. Hawker, Evolution of block copolymer lithography to highly ordered square arrays. Science 322, 429–432 (2008).
- C. Tang, K. Sivanandan, B. C. Stahl, G. H. Fredrickson, E. J. Kramer, C. J. Hawker, Multiple nanoscale templates by orthogonal degradation of a supramolecular block copolymer lithographic system. ACS Nano 4, 285–291 (2010).
- S.-M. Park, G. S. W. Craig, Y.-H. La, H. H. Solak, P. F. Nealey, Square arrays of vertical cylinders of PS-b-PMMA on chemically nanopatterned surfaces. *Macromolecules* 40, 5084–5094 (2007).
- J. H. Mun, S. K. Cha, Y. C. Kim, T. Yun, Y. J. Choi, H. M. Jin, J. E. Lee, H. U. Jeon, S. Y. Kim,
 O. Kim, Controlled segmentation of metal nanowire array by block copolymer lithography and reversible ion loading. *Small* 13, 1603939 (2017).
- 31. R. Liu, H. Huang, Z. Sun, A. Alexander-Katz, C. A. Ross, Metallic nanomeshes fabricated by multimechanism directed self-assembly. *ACS Nano* **15**, 16266–16276 (2021).
- 32. Z. Ma, C. Chen, X. Cui, L. Zeng, L. Wang, W. Jiang, J. Shi, Hydrogen evolution/oxidation electrocatalysts by the self-activation of amorphous platinum. *ACS Appl. Mater. Interfaces* 13, 44224–44233 (2021).
- L. A. Kibler, J. M. Hermann, A. Abdelrahman, A. A. El-Aziz, T. Jacob, New insights on hydrogen evolution at Au single crystal electrodes. *Curr. Opin. Electrochem.* 9, 265–270 (2018).
- A. Devi, H. Minhas, L. Sahoo, Rashi, S. Gratious, A. Das, S. Mandal, B. Pathak, A. Patra, Insights of the efficient hydrogen evolution reaction performance in bimetallic Au₄Cu₂ nanoclusters. *Nanoscale* 16, 1758–1769 (2024).
- W. Chen, Y. Shi, C. Liu, Z. Ren, Z. Huang, Z. Chen, X. Zhang, S. Liang, L. Xie, C. Lian, G. Qian, J. Zhang, X. Liu, D. Chen, X. Zhou, W. Yuan, X. Duan, Restructuring the interfacial active sites to generalize the volcano curves for platinum-cobalt synergistic catalysis. *Nat. Commun.* 15, 8995 (2024).
- F. Guo, T. J. Macdonald, A. J. Sobrido, L. Liu, J. Feng, G. He, Recent advances in ultralow-Pt-loading electrocatalysts for the efficient hydrogen evolution. *Adv. Sci.* 10, 2301098 (2023).
- F. A. Detcheverry, H. Kang, K. C. Daoulas, M. Müller, P. F. Nealey, J. J. de Pablo, Monte Carlo simulations of a coarse grain model for block copolymers and nanocomposites. *Macromolecules* 41, 4989–5001 (2008).
- M. Hömberg, M. Müller, Main phase transition in lipid bilayers: Phase coexistence and line tension in a soft, solvent-free, coarse-grained model. J. Chem. Phys. 132, 155104 (2010).
- F. A. Detcheverry, D. Q. Pike, P. F. Nealey, M. Müller, J. J. de Pablo, Monte Carlo simulation of coarse grain polymeric systems. *Phys. Rev. Lett.* 102, 197801 (2009).
- J. Park, A. Ramírez-Hernández, V. Thapar, S.-M. Hur, Mesoscale simulations of polymer solution self-assembly: Selection of model parameters within an implicit solvent approximation. *Polymers* 13, 953 (2021).
- J. A. Anderson, J. Glaser, S. C. Glotzer, HOOMD-blue: A Python package for highperformance molecular dynamics and hard particle Monte Carlo simulations. *Comput. Mater. Sci.* 173, 109363 (2020).
- A. P. Thompson, H. Metin Aktulga, R. Berger, D. S. Bolintineanu, W. Michael Brown,
 P. S. Crozier, P. J. in 't Veld, A. Kohlmeyer, S. G. Moore, T. D. Nguyen, R. Shan, M. J. Stevens,
 J. Tranchida, C. Trott, S. J. Plimpton, LAMMPS A flexible simulation tool for particle-based materials modeling at the atomic, meso, and continuum scales. *Comput. Phys. Commun.* 271, 108171 (2022).
- J. Ahrens, B. Geveci, C. Law, ParaView: An End-User Tool for Large Data Visualization, in Visualization Handbook (2005).
- M. Ester, H.-P. Kriegel, J. Sander, X. Xu, "A density-based algorithm for discovering clusters in large spatial databases with noise," in KDD'96: Proceedings of the Second International Conference on Knowledge Discovery and Data Mining, (1996), pp. 226–231.
- 45. E. Schubert, J. Sander, M. Ester, H. P. Kriegel, X. Xu, DBSCAN revisited, revisited: Why and how you should (still) use DBSCAN. ACM Trans. Database Syst. 42, 19 (2017).
- D. R. Nelson, B. I. Halperin, Dislocation-mediated melting in two dimensions. *Phys. Rev. B: Condens. Matter* 19, 2457–2484 (1979).

Acknowledgments: The Institute of Engineering Research at Seoul National University provided research facilities for this work. We appreciate M. Lee and J. Park for technical assistance with sample preparation. **Funding:** This work was supported by National Research

SCIENCE ADVANCES | RESEARCH ARTICLE

Foundation of Korea (NRF) grants funded by Korea Government (MSIT) 2021R1A2C2007339 and 2021R1A2C2013684. This work is also supported by the Samsung Research Funding Center for Samsung Electronics under project number SRFC-MA2201-02. **Author contributions:** Conceptualization: S.E.K. and S.Y.K. Overall experiment: S.E.K. Molecular dynamics simulation: G.P.I., V.T., and S.-M.H. Hydrogen evolution reaction experiment: H.W.K., H.G.K., and J.R. Supervision: J.R., S.-M.H., and S.Y.K. Writing—original draft: All authors. **Competing interests:** The authors declare that they have no competing interests. **Data and**

materials availability: All data needed to evaluate the conclusions in the paper are present in the paper and/or the Supplementary Materials.

Submitted 4 March 2025 Accepted 24 June 2025 Published 23 July 2025 10.1126/sciadv.adx1235